3D FIB-SEM reconstruction of microtubule-organelle interaction in whole primary mouse beta cells

Andreas Müller[1,2,3,✉], Deborah Schmidt[4,5], C. Shan Xu[6], Song Pang[6], Joyson Verner D'Costa[1,2,3], Susanne Kretschmar[7], Carla Münster[1,2,3], Thomas Kurth[7], Florian Jug[4,5,8], Martin Weigert[9,†], Harald F. Hess[6,†], and Michele Solimena[1,2,3,5,†,✉]

[1]Molecular Diabetology, University Hospital and Faculty of Medicine Carl Gustav Carus, TU Dresden, Dresden, Germany
[2]Paul Langerhans Institute Dresden (PLID) of the Helmholtz Center Munich at the University Hospital Carl Gustav Carus and Faculty of Medicine of the TU Dresden, Dresden, Germany
[3]German Center for Diabetes Research (DZD e.V.), Neuherberg, Germany
[4]Center for Systems Biology Dresden (CSBD), Dresden, Germany
[5]Max-Planck Institute of Molecular Cell Biology and Genetics, Dresden, Germany
[6]Janelia Research Campus, Howard Hughes Medical Institute, Ashburn, VA, USA
[7]Center for Molecular and Cellular Bioengineering (CMCB), Technology Platform, TU Dresden, Dresden, Germany
[8]Fondazione Human Technopole, Milano, Italy
[9]Institute of Bioengineering, School of Life Sciences, École polytechnique fédérale de Lausanne (EPFL), Lausanne, Switzerland
[†]Equal contribution.

Microtubules play a major role in intracellular trafficking of vesicles in endocrine cells. Detailed knowledge of microtubule organization and their relation to other cell constituents is crucial for understanding cell function. However, their role in insulin transport and secretion is currently under debate. Here, we use FIB-SEM to image islet beta cells in their entirety with unprecedented resolution. We reconstruct mitochondria, Golgi apparati, centrioles, insulin secretory granules and microtubules of seven beta cells, and generate a comprehensive spatial map of microtubule-organelle interactions. We find that microtubules form non-radial networks that are predominantly not connected to either centrioles or endomembranes. Microtubule number and length, but not microtubule polymer density, vary with glucose stimulation. Furthermore, insulin secretory granules are enriched near the plasma membrane where they associate with microtubules. In summary, we provide the first 3D reconstructions of complete microtubule networks in primary mammalian cells together with evidence regarding their importance for insulin secretory granule positioning and thus supportive role in insulin secretion.

Correspondence:
andreas.mueller1@tu-dresden.de,
michele.solimena@uniklinikum-dresden.de

Introduction

Cytoskeletal elements, such as microtubules or actin filaments, play a pivotal role in regulating peptide hormone trafficking and secretion in endocrine cells (Rudolf et al., 2001; Park and Loh, 2008; Fourriere et al., 2020). In pancreatic islet beta cells, for example, insulin secretion induced upon elevated levels of blood glucose is accompanied by increased polymerization of tubulin (Pipeleers et al., 1976; McDaniel et al., 1980; Heaslip et al., 2014) and a loosening of cortical F-actin (Kalwat and Thurmond, 2013). Beta cells contain several thousand insulin secretory granules (SGs) (Fava et al., 2012) of which 10-20% are dynamically transported along microtubules (Hoboth et al., 2015) and 1-2% are undergoing exocytosis upon glucose stimulation (Rorsman and Renström, 2003). An intact microtubule network (Boyd et al.,

1982) as well as motor-mediated transport of SGs are necessary for insulin secretion (Meng et al., 1997; Varadi et al., 2002; Cui et al., 2011) and this active transport increases after stimulation with glucose (Pouli et al., 1998; Hoboth et al., 2015; Müller et al., 2017a). However, in contrast to these data microtubules have also been postulated to hinder insulin SG transport under low glucose, whereas a loosening of the microtubule network upon glucose stimulation allows SGs to reach the plasma membrane (Zhu et al., 2015). In view of these considerations it is therefore crucial to obtain high resolution data on microtubule remodelling and insulin SG interaction.

Previous studies by fluorescence light microscopy showed that the organization of the beta cell microtubule network resembles a tangled, non-directional scaffold (Varadi et al., 2003; Zhu et al., 2015), rather than the radial organization found in tumor cell lines (Meiring et al., 2020). However, even advanced super resolution methods cannot provide the resolution and field of view necessary to accurately reconstruct the 3D microtubule network in whole cells, since microtubules have an outer diameter of approximately 25 nm and primary beta cells are relatively large cells (10-20 μm in diameter) that are densely embedded in the islets of Langerhans. In contrast, electron microscopy methods allow nanometer resolution imaging of microtubules together with all other cell structures and organelles. For example, serial-section electron tomography has been used to reconstruct the several thousand microtubules of mitotic spindles in *C. elegans* (Redemann et al., 2017) and the 3D microtubule network of yeast cells in interphase (Höög et al., 2007). Recently, block-face scanning electron microscopy has been used to reconstruct microtubules of chemically fixed mitotic spindles of HeLa cells followed by spatial analysis (Nixon et al., 2017). However, high resolution 3D reconstructions of the microtubule network in whole primary mammalian cells in interphase have, to our knowledge, never been reported. Here, we applied high resolution, near-isotropic focused ion
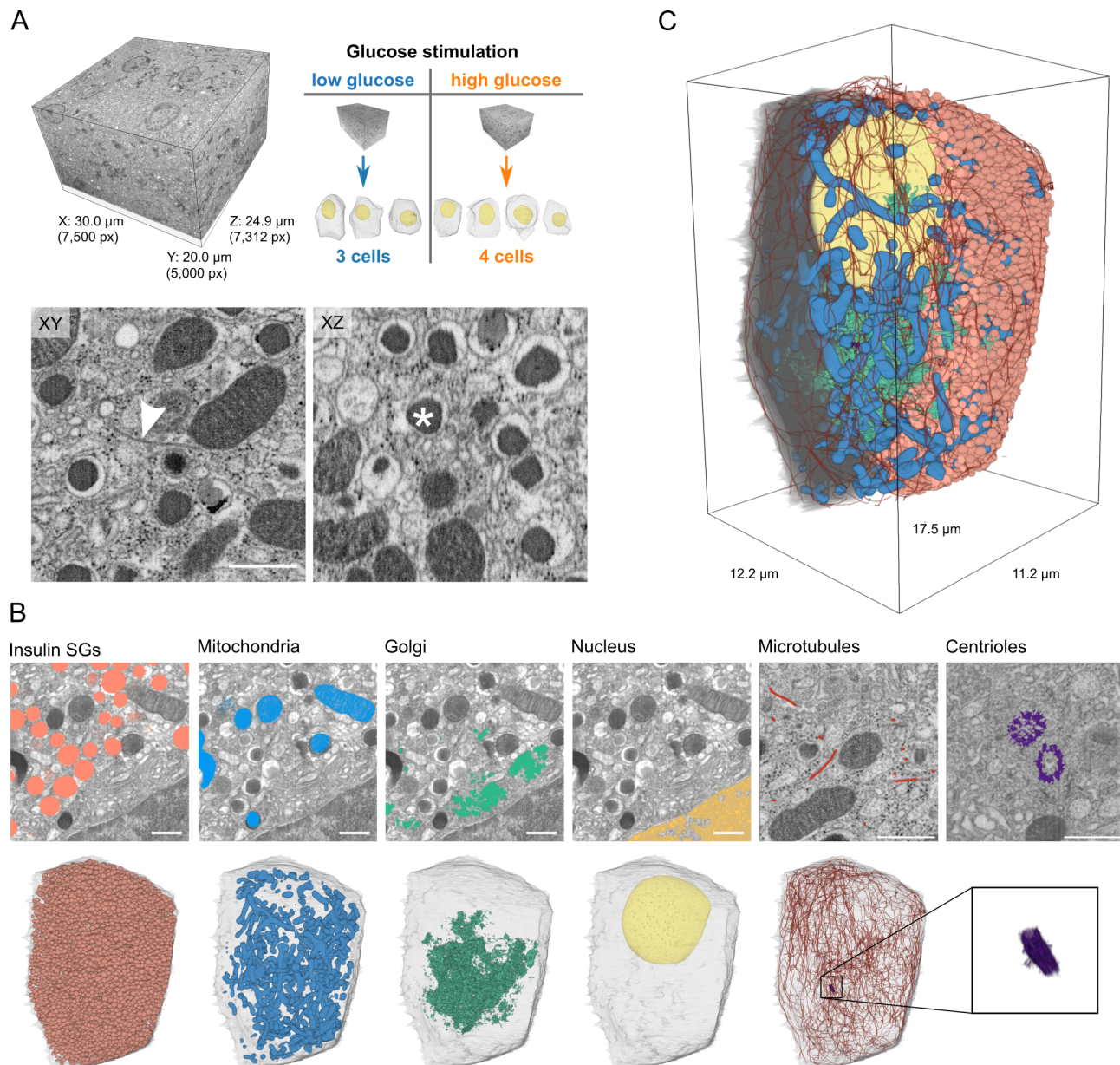
Fig. 1. FIB-SEM volumes of pancreatic beta cells and 3D segmentation of microtubules and organelles. A) Full FIB-SEM volume of a pancreatic islet (left), one of which was acquired for low and high glucose conditions containing 3 (low) and 4 (high) complete beta cells (right). Shown are the lateral (XY) and axial (XZ) views of a small crop, highlighting the quasi-isotropic resolution of the FIB-SEM volumes, the arrowhead indicates a microtubule, the asterisk an insulin secretory granule (SG). Scale bar: 500 nm **B)** Raw lateral images with segmentation overlay for insulin SGs, mitochondria, Golgi apparatus, nucleus (of the identical region) and microtubules and centrioles (of different regions). Below the overlays we show 3D renderings of the corresponding organelles of one whole cell (high glucose condition) accompanied by a transparent rendering of the plasma membrane. Centrioles are magnified in the last panel. Scale bars: 500 nm. **C)** 3D rendering of one cell containing all segmented organelles. The plasma membrane and insulin SGs were removed in the left half of the cell to help visualizing its inner parts.

beam scanning electron microscopy (FIB-SEM) to image large volumes of cryo-immobilized, resin-embedded pancreatic islets under different glucose stimuli. We provide the first reconstructions of the full 3D microtubule network within primary mammalian cells, comprising 7 cells in total. We show that beta cell microtubules are predominantly not connected to the centrioles and endomembranes and form a non-radial network. We show that glucose stimulation induces microtubule remodelling, which, however, does not change the overall polymerized tubulin density. We additionally reconstruct insulin SGs, Golgi, plasma membranes, nuclei, mitochondria, and centrioles of all cells and perform a compre-

hensive quantitative spatial analysis of microtubule-organelle interaction. Our data show an enrichment of insulin SGs together with microtubules near the plasma membrane, pointing to the role of microtubules for supporting the secretory functionality in beta cells.

Results and Discussion

High resolution FIB-SEM resolves organelles and microtubules

In order to achieve near-isotropic image resolution at high throughput we used an enhanced FIB-SEM setup (Xu et al., 2017, 2020c) to image large volumes of isolated pancreatic islets of Langerhans treated with low (resting) or high glu-
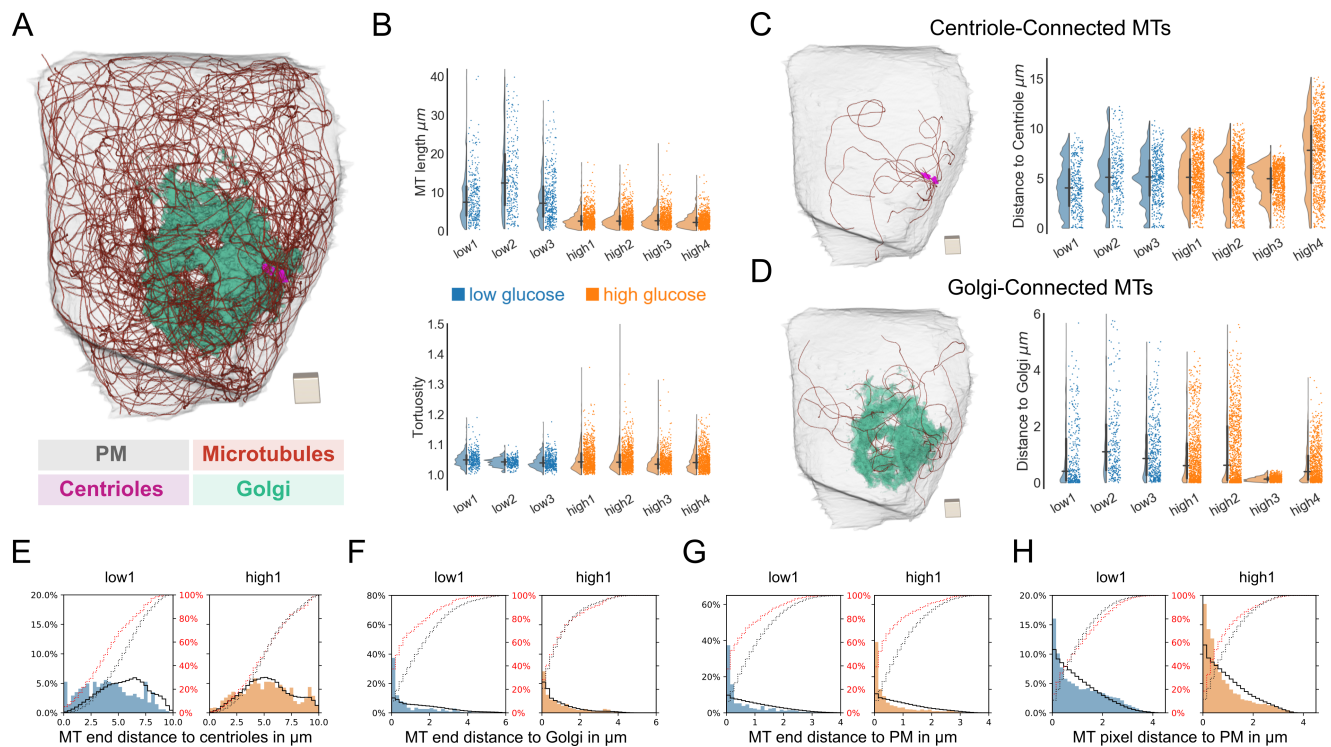
Fig. 2. Microtubule network properties and distance distributions. A) Fully reconstructed microtubule network of one beta cell with microtubules in red, centrioles in purple, Golgi apparatus in green and plasma membrane (PM) in gray transparent. Scale: cube with a side-length of 1 µm. **B)** Microtubule (MT) length and tortuosity distribution of all 7 analyzed cells (blue: low glucose cells, orange: high glucose cells). Horizontal and vertical lines signify the mean and the interquartile range, respectively. **C)** Rendering of only centriole-connected (centrosomal) microtubules of the same cell as in A. The plots show the distributions of distances of MT ends to centrioles for all analyzed cells. Scale: cube with a side-length of 1 µm. **D)** Rendering of only Golgi-connected microtubules of the same cell as in A. Scale: cube with a side-length of 1 µm. The plots show the distributions of distances of the microtubule ends to Golgi for all analyzed cells. **E)** Distribution of the distance of microtubule ends to centrioles for one representative low glucose (blue) and one high glucose (orange) cell with random distributions ρ_{Cent} represented by a black line. Red dotted and black dotted lines represent actual and random cumulative distributions, respectively. **F)** Distribution of the distance of microtubule ends to Golgi membranes for the same cells as in E with random distributions ρ_{Golgi} represented by a black line. Red dotted and black dotted lines represent actual and random cumulative distributions, respectively. **G)** Distribution of the distance of microtubule ends to the plasma membrane for for the same cells as in E with random distributions ρ_{PM} represented by a black line. Red dotted and black dotted lines represent actual and random cumulative distributions, respectively. **H)** Distribution of the distance of microtubule pixels to the plasma membrane for the same cells as in E with random distributions ρ_{PM} represented by a black line. Red dotted and black dotted lines represent actual and random cumulative distributions, respectively.

cose (stimulating insulin secretion) concentrations. Samples were first fixed by high pressure freezing followed by a novel freeze substitution protocol adapted from (Hall et al., 2013) to improve image contrast compared to previously applied freeze substitution protocols (Verkade, 2008; Müller et al., 2017b). Crucially, this improved contrast allowed to reliably detect microtubules together with all major organelles (Fig. 1A, Supp. Fig. 1A, C, D). We acquired two volumes (one for each glucose condition) of Durcupan embedded isolated islets containing several full beta cells at near-isotropic 4 nm voxel size (Fig. 1A, Supp. Fig. 1B; Video 1). Specifically, imaging took approximately two weeks per stack resulting in two large volumes with pixel dimensions of 4,900×5,000×7,570 pixels for the low glucose and 7,500×5,000×7,312 pixels for the high glucose sample with file sizes of 176 and 255 GB, respectively. Acquisition of large volumes combined with high resolution was essential to obtain 3D stacks containing several beta cells and to simultaneously resolve microtubules. We then applied manual as well as machine learning-based 3D segmentation to trace microtubules and reconstruct organelles such as the insulin SGs, mitochondria, centrioles with axonemes of the primary cilia, nuclei, the Golgi apparatus and plasma membrane (Fig. 1B). Microtubules were segmented manually by

creating a skeleton with KNOSSOS (Helmstaedter et al., 2011). Plasma membranes, nuclei and centrioles of individual cells were segmented with Microscopy Image Browser (Belevich et al., 2016). Mitochondria were semi-automatically segmented with ilastik (Berg et al., 2019) whereas insulin SGs were automatically detected with STARDIST (Weigert et al., 2020). The cisternae of the Golgi apparatus were automatically segmented by a U-Net (Ronneberger et al., 2015) that was trained with ground truth annotations of small crops from the original FIB-SEM volumes. The Golgi apparatus of beta cells has in part been reconstructed at high detail (Marsh et al., 2001). Our segmentation was focused on Golgi cisternae and therefore does not include most Golgi vesicles. However, it provides a precise localization of Golgi membrane stacks which was necessary to investigate microtubule interaction. In total we obtained full microtubule and organelle segmentations for 7 mostly complete beta cells (3 for the low glucose and 4 for the high glucose condition), that provided the basis for the subsequent visualization and analysis in 3D (Fig. 1C, Supp. Fig. 2, Video 2, Video abstract). We found that all cells except for one (high glucose cell 3, Supp. Fig. 2) were similar in their general ultrastructure and segmentation features. This particular cell, however, showed signs of stress, such as irregular cell and nucleus

Glucose status	Low glucose			High glucose			
	Cell 1	Cell 2	Cell 3	Cell 1	Cell 2	Cell 3	Cell 4
Cell volume in μm^3	799	997	927	1,010	834	898	793
Nucleus volume in μm^3	115	150	148	126	116	102	106
Nucleus volume percentage	14.4%	15.0%	16.0%	12.5%	13.9%	11.4%	13.4%
Mitochondria total volume in μm^3	73	50	104	68	82	44	98
Mitochondria total volume percentage	9.1%	5.0%	11.2%	6.7%	9.9%	4.9%	12.4%
Golgi volume in μm^3	18	8	8	22	18	12	13
Golgi volume percentage	2.2%	0.8%	0.9%	2.2%	2.1%	1.3%	1.6%
Insulin SG number	5,139	9,947	4,073	9,714	7,289	13,812	9,310
Insulin SG total volume in μm^3	133	210	108	208	153	254	152
Insulin SG total volume percentage	16.6%	21.0%	11.6%	20.6%	18.4%	28.3%	19.1%
Insulin SG average volume in μm^3	0.026	0.021	0.027	0.022	0.021	0.019	0.016
Insulin SG average surface area in μm^2	0.419	0.367	0.426	0.369	0.366	0.337	0.309
Insulin SG average diameter in μm	0.409	0.383	0.413	0.384	0.384	0.368	0.355
Insulin SG assoc. with MT in % of all SG	30.7%	34.4%	37.3%	29.1%	39.0%	28.7%	27.0%
Assoc. insulin SG close to PM ($\leq$ 500 nm) in %	53.0%	45.3%	59.2%	56.6%	55.4%	51.2%	62.1%
Not-assoc. insulin SG close to PM ($\leq$ 500 nm) in %	50.6%	44.4%	51.5%	41.7%	49.5%	25.3%	59.6%
Microtubule number	342	291	440	1,007	1,101	862	932
Microtubule average length in μm	8.82	14.63	8.54	3.10	3.14	3.25	2.66
Microtubule cumulative length in μm	3,018	4,260	3,756	3,115	3,452	2,799	2,479
Microtubule average tortuosity	1.05	1.04	1.04	1.05	1.05	1.04	1.05
Microtubule centriole-connected percentage	3.5%	2.7%	3.9%	0.7%	1.7%	0.7%	1.3%
Microtubule Golgi-connected percentage	9.6%	0.3%	0.5%	3.7%	10.2%	3.0%	3.2%

Table 1. Quantitative microtubule and organelle measurements of all cells. Volumes of the analysed cells, nuclei, mitochondria, Golgi apparati, insulin SGs. Insulin SG numbers and individual volumes. Numbers and percentages of microtubule-associated and not associated SGs. Numbers, average and cumulative lengths and tortuosity of microtubules. Percentages of centrosomal and Golgi-connected microtubules.

shape and a fragmented Golgi apparatus. Nevertheless, we decided to provide all data of this cell and to discuss them in the text where necessary.

To facilitate navigation of our results, we developed the tool *BetaSeg Viewer*, a FIJI plugin based on BigDataViewer (Pietzsch et al., 2015). *BetaSeg Viewer* enables the joint view of both raw volume and organelle segmentation masks (together with their associated properties), hence an easy and intuitive access to the data (*cf*. Supp. Fig. 1E, F, Video 3). All segmentation masks and preprocessed data for each individual cell together with the original raw image stacks are publicly available.

Beta cell microtubule number and length vary with glucose stimulation

In order to investigate the remodelling of the microtubule network upon stimulation with glucose we first quantified basic microtubule properties for low as well as high glucose conditions (Fig. 2). The total number of reconstructed microtubules per cell was between 291 and 440 for low glucose cells, and between 862 to 1,101 for high glucose cells, implying a substantial increase of microtubule number in glucose stimulated cells (Table 1). In contrast, the average microtubule length for low glucose cells ranged from 8.54 to 14.63 µm, which is greater than that of high glucose cells where it ranged from 2.66 to 3.25 µm (Fig. 2B, Table 1). Interestingly, the cumulative microtubule length

per cell showed only modest variation between glucose conditions with 3,018 to 4,260 µm in low glucose and 2,479 to 3,452 µm in high glucose cells (Table 1). We additionally computed the tortuosity (curvature) along each microtubule, and found no major differences between microtubules in low and high glucose cells (Fig. 2B). The much shorter microtubule length in high glucose cells might be due to changes in microtubule dynamics upon glucose stimulation leading to shorter microtubules (Brouhard and Rice, 2018). It has been proposed that high glucose leads to depolymerization of microtubules while simultaneously new microtubules are being generated (Zhu et al., 2015). Alternatively, glucose-induced activation of severing enzymes such as spastin and katanin could lead to shorter microtubules. Notably, both spastin and katanin are AAA ATPases (Hartman et al., 1998; Roll-Mecak and Vale, 2008) that could be sensitive to the increased ATP/ADP ratio induced by glucose stimulation.

Beta cell microtubules form non-connected networks and are enriched near the plasma membrane

We next investigated for each cell the connectivity of the reconstructed microtubule network to different cell organelles. Our segmentation allowed for precise localization of microtubule ends (Supp. Fig. 1C) allowing for investigating their connectivity to centrioles and endomembranes. In the case of centrioles, we defined a single microtubule to be centriole-connected or *centrosomal*, if one of its ends is lo-
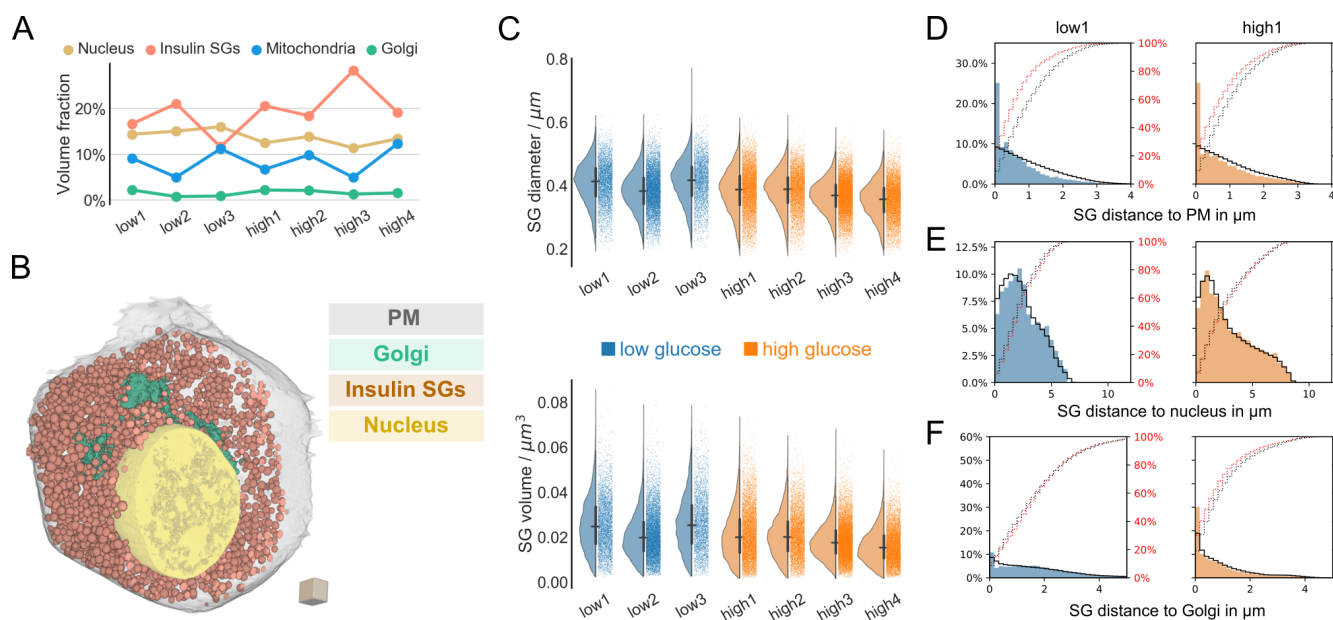
Fig. 3. Insulin SG properties and distance distributions. A) Volume fraction (percentage) of segmented organelles for all analyzed cells. **B)** 3D rendering of one beta cell with plasma membrane (transparent gray), insulin SGs (orange), Golgi apparatus (green) and nucleus (yellow). Scale: cube with a side-length of 1 µm. **C)** Diameter and volume distributions of insulin SGs of all 7 analyzed cells (blue: low glucose cells, orange: high glucose cells). Horizontal and vertical lines signify the mean and the interquartile range, respectively. **D)** Distribution of the distance of insulin SGs to the plasma membrane (PM) for one representative low glucose (blue) and one high glucose (orange) cell with random distributions ρ_{PM} represented by a black line. Red dotted and black dotted lines represent actual and random cumulative distributions, respectively. **E)** Distribution of the distance of insulin SGs to the nucleus for one representative low glucose (blue) and one high glucose (orange) cell with random distributions ρ_{Nuc} represented by a black line. Red dotted and black dotted lines represent actual and random cumulative distributions, respectively. **F)** Distribution of the distance of insulin SGs to the Golgi apparatus for one representative low glucose (blue) and one high glucose (orange) cell with random distributions ρ_{Golgi} represented by a black line. Red dotted and black dotted lines represent actual and random cumulative distributions, respectively.

cated within the pericentriolar material (approximately 200 nm around the centrioles). Notably, for all cells only few microtubules were centriole-connected, with a total number ranging from 8 to 17 in low glucose and from 6 to 19 in high glucose cells, corresponding to 2.7 to 3.9% (low glucose) and 0.7 to 1.7% (high glucose) centrosomal microtubules (Fig. 2C, Table 1, Video 4). This demonstrates that the microtubule network in mouse beta cells is distinctly non-centrosomal irrespective of either glucose condition. Previous studies (Zhu et al., 2015) have indicated that a significant number of microtubules are connected to the Golgi apparatus shortly after microtubule depolymerization by nocodazole. Golgi-derived microtubules originate directly from Golgi membranes (Chabin-Brion et al., 2001; Efimov et al., 2007; Sanders and Kaverina, 2015) and mechanisms for their generation include recruitment of γ-TuRC to Golgi membranes with the help of CLASPs (Efimov et al., 2007) or AKAP450 (Sanders and Kaverina, 2015). Therefore, we chose a threshold of 20 nm in order to define microtubules that are structurally connected to the Golgi apparatus (Golgi-connected). We found that between 2 and 10% of all microtubules were Golgi-connected (Fig. 2D, Table 1, Video 5), while the distance distribution of microtubule ends to the Golgi peaked at smaller values compared to the centrioles (Fig. 2C, D, Supp. Fig. 3A, B, C). To investigate whether this might be due to the expanded sponge-like geometry of the Golgi rather than the microtubule end distribution itself, we computed for each cell a corresponding *random golgi distribution* ρ_{Golgi}, *i.e.* the distribution of distances from the Golgi to all other points inside the cell subvolume excluding

the nucleus. That way ρ_{Golgi} captures the purely geometric effects of the spatial Golgi arrangement and allows an estimate of the distance distribution of the hypothetical case of randomly positioned microtubule ends. We found that the distributions of microtubule end distance to the Golgi were slightly shifted towards smaller values compared to ρ_{Golgi} for both glucose conditions (Fig. 2F, Supp. Fig. 3B, C). This distribution was heterogeneous between cells. While some cells exhibited a considerable fraction of microtubule ends that are close to the Golgi (low glucose 1, high glucose 2 and 4) such an enrichment was not observed in other cells (low glucose 2 and 3, high glucose 1, *cf*. Supp. Fig. 3B). A high density of microtubule ends that are close, yet structurally not connected, to Golgi membranes indicates that these microtubules might have originated from the Golgi, but have lost their connection to it. In contrast, the distance distribution of microtubule ends to the centrioles was more similar to the respective ρ_{Cent} (Fig. 2E, Supp. Fig. 3A). One cell (high glucose cell 3) showed a highly fragmented Golgi (Supp. Fig. 2), which led to a strongly enriched distribution of microtubule ends close to Golgi membranes (Fig. 2D, Supp. Fig. 2, Supp. Fig. 3B, C). However, the fraction of Golgi connected microtubules was similar to that of the other cells and the distribution of microtubule ends can be explained by the fragmentation of the Golgi apparatus itself.

Surprisingly, independent of glucose concentration there was stronger enrichment of microtubule ends close the plasma membrane compared to its random distribution ρ_{PM} in all cells (Fig. 2G, Supp. Fig. 3D). Moreover, microtubule pixels were also enriched near the plasma membrane (Fig. 2H,

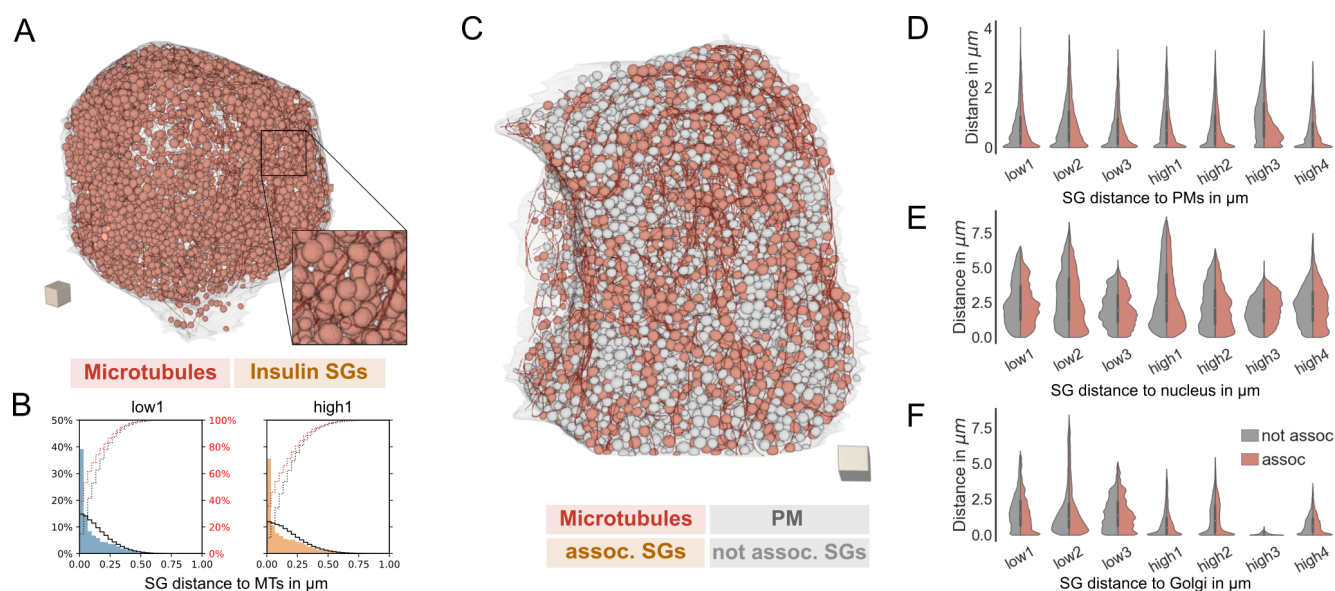**Fig. 4. Spatial association between microtubules and insulin SGs. A)** 3D rendering of a cell with plasma membrane (transparent gray), microtubules (red) and insulin SGs (orange). Inset shows a magnified region. Scale: cube with a side-length of 1 μm. **B)** Distribution of the distance of insulin SGs to microtubules (MTs) for one representative low glucose (blue) and one high glucose (orange) cell with random distributions ρ_{MT} represented by a black line. Red dotted and black dotted lines represent actual and random cumulative distributions, respectively. **C)** 3D rendering of a cell with plasma membrane, microtubule-associated SGs (orange), not associated SGs (light gray), and microtubules (red). Scale: cube with a side-length of 1 μm. **D)** Violin plots depicting the distance of associated and not associated insulin SGs to the plasma membrane (PM). **E)** Violin plots depicting the distance of associated and not associated insulin SGs to the nucleus. **F)** Violin plots depicting the distance of associated and not associated insulin SGs to the Golgi apparatus.

Supp. Fig. 3E). Notably we did not find major differences in polymerized tubulin density between glucose conditions (Fig. 2H, Supp. Fig. 3E). Our findings show that although a small number of microtubules is connected to centrioles and Golgi apparatus a majority of over 80% of all microtubules are disconnected from these compartments. Although both Golgi apparatus and centrioles could still serve as microtubule organizing centers, our data suggest either other places of microtubule generation or severing of microtubules after their generation. Notably, a significant body of literature indicates that microtubules can appear spontaneously in the cytosol (Vorobjev et al., 1997; Yvon and Wadsworth, 1997). In order to stabilize these microtubules proteins such as CAMSAP2 (Jiang et al., 2014) or anchoring proteins such as Ninein (Mogensen et al., 2000) are necessary and might play a role in beta cells.

Finally, the observed remodelling towards shorter microtubules under glucose stimulation did not alter the polymerized tubulin density in general.

Organelle fractions are heterogeneous across cells

To gain insight into the role of microtubules in organelle positioning we reconstructed insulin SGs, mitochondria, plasma membranes, centrioles with axonemes of the primary cilia, Golgi apparati and nuclei of all 7 cells (Supp. Fig. 2, Table 1, Video 2). Quantification of these organelles showed a clear heterogeneity among the cells, independent of glucose stimulation (Table 1). The volumes of the cells were variable, ranging from 799 to 997 μm³ in the low glucose cells and from 793 to 1,010 μm³ in the high glucose cells. Mitochondria volumes ranged from 50 to 104 μm³ for low glucose and from 44 to 98 μm³ for high glucose cells. The volume of the nuclei ranged from 102 to 150 μm³ in the 6 cells containing

complete nuclei. The number of insulin SGs was especially variable with only 4,073 SGs in one of the low glucose cells and up to 13,812 SGs in one high glucose cell. These data span the entire range of values that so far had been calculated for an average beta cell using either stereological methods (Dean, 1973; Olofsson et al., 2002; Shomorony et al., 2015) or in-silico modelling (Fava et al., 2012). Our data clearly demonstrate a strong heterogeneity of beta cells in the number of their SGs independent of glucose stimulation. This is in agreement with (Noske et al., 2008) who observed substantial organelle heterogeneity between two beta cells reconstructed with serial section electron tomography (however without considering microtubules due to limited resolution). In order to investigate if the differences in SG number were correlated with cell size we calculated the volume fractions of insulin SGs, and additionally of the nuclei, Golgi apparati and mitochondria. While nuclei and Golgi fractions were relatively stable across cells, volume fractions of mitochondria and insulin SGs were highly variable even within same glucose conditions (cf. Fig. 3A): for insulin SGs the volume fraction ranged from 11.6 to 28.8%, demonstrating that insulin SG number does not directly correlate with cell volume.

Insulin SGs are enriched near the plasma membrane, but not the nucleus, independent of glucose concentration

Next, we wondered if the observed beta cell heterogeneity would also be reflected in insulin SG distribution and interaction with other organelles. Our 3D high-resolution reconstructions allowed for a quantitative analysis of insulin SGs and their spatial distribution and interaction with the plasma membrane, nucleus and Golgi apparatus (Fig. 3B). In total we analyzed the precise segmentation masks of >60,000 insulin

SGs for all cells. First, we calculated SG volumes, surface areas, diameters and sphericity for all SGs in our cells (Fig. 3C, Supp. Fig. 3F, G). The average SG volume ranged between 0.016 to 0.026 μm^3 and the SG surface area between 0.309 to 0.429 μm^2. Insulin SGs in all cells were close to spherical in shape (Supp. Fig. 3G) with a mean diameter between 355 and 413 nm (Fig. 3C), comparable to values obtained by stereological methods (Dean, 1973; Olofsson et al., 2002). Next, we investigated the distance distribution of insulin SGs to the plasma membrane. As before, we also computed the corresponding random distributions ρ_{PM} for comparison. As can be inferred from Fig. 3D and Supp. Fig. 3H, especially SGs closest to the plasma membrane are substantially over-represented when compared to ρ_{PM}. We observed this phenomenon in all cells including the ones with a smaller fraction of insulin SGs. In contrast, SG distances from the nucleus followed approximately the random distributions ρ_{Nuc} in all cells (Fig. 3E, Supp. Fig. 3I). Interestingly, the insulin SG distance to Golgi distribution in low glucose cells followed the random distributions ρ_{Golgi}, whereas under high glucose conditions SG were slightly enriched near the Golgi indicative of the production of new SGs (Fig. 3F, Supp. Fig. 3J). We therefore conclude that SGs are enriched near the plasma membrane under both low and high glucose conditions, but not near the nucleus.

Insulin SGs associate with microtubules close to the plasma membrane

The strong enrichment of insulin SGs at the plasma membrane led us to investigate the distance distribution and direct association of both organelles (Fig. 4A). Interestingly, insulin SGs were strongly enriched close to microtubules when compared to random microtubule distributions ρ_{MT} in all cells independently of glucose concentration (Fig. 4B, Supp. Fig. 3K). Furthermore, a high percentage of SGs was directly associated with microtubules in both glucose conditions. We found between 31 and 37% of associated SGs in low glucose cells and between 27 and 39% in high glucose cells (Fig. 4C, Table 1, Supp. Fig. 2, Video 6). This corresponded to 1.95 to 4.04 microtubule-associated SGs per μm^3 of cytoplasmic volume in low glucose (rested) cells and 3.20 to 4.98 microtubule-associated SGs per μm^3 of cytoplasmic volume in glucose stimulated cells. Furthermore, the majority of microtubule-associated SGs were located close to the plasma membrane (Fig. 4D). Interestingly, the fraction of microtubule-associated SGs at the plasma membrane within a distance of 500 nm was as high or higher than the fraction of not associated SGs, independent of glucose stimulation (Table 1). The distance distribution of microtubule-assocciated and not associated SGs from the nucleus and Golgi apparatus was more heterogeneous with some cells showing a higher percentage of associated SGs close to these organelles and others a higher percentage of not connected SGs (Fig. 4E, F). Together with the data on microtubule and SG distribution these findings indicate an active role of microtubules in maintaining the enrichment of insulin SGs in the cell periphery.

Summary

We provide here the first 3D reconstructions of all microtubules in primary mammalian cells in interphase using pancreatic beta cells as a model system. Although, electron microscopy can only give snapshots of the cell's ultrastructure, our data provide unprecedented insights into the 3D microtubule organisation and organelle interaction with nanometer precision. We found that a minority of microtubules are connected to the centrioles and Golgi apparatus, while most of the microtubules appear to be freely positioned within the cytosol. The presence of largely non-radial, disconnected microtubule networks is a key feature of differentiated cells (Muroyama and Lechler, 2017) and implies a major microtubule remodelling during beta cell development. Notably, immature beta cells that proliferate have a lower secretory capacity compared to mature beta cells (Salinno et al., 2019). Microtubule remodelling combined with a change in microtubule purpose, *i.e.* from spindle formation to membrane trafficking, could contribute to the increased beta cell functionality. We furthermore found substantial differences in microtubule number and length between low and high glucose conditions suggesting a major remodelling of the microtubule network upon glucose stimulation. However, in contrast to (Zhu et al., 2015) we did not measure changes in density of polymerized tubulin between glucose conditions, questioning the proposed hindering role of microtubules for SG mobility in low glucose. Moreover, in all cells microtubules as well as insulin SGs were enriched near the plasma membrane implying the role of microtubules in maintaining organelle positioning (de Forges et al., 2012). Interestingly, the fraction of insulin SGs directly connected to microtubules was between 20 and 40% regardless of glucose treatment. Thus, microtubules likely maintain a high density of insulin SGs near the plasma membrane under low as well as under high glucose conditions keeping insulin SGs in close proximity to secretion sites. In conclusion, our data provide quantitative insights into the ultrastructure of beta cells and the reciprocal interaction among their compartments at an unprecedented resolution. This detailed knowledge will facilitate our understanding of beta cell function and insulin trafficking.

Data and software availability

Segmentation masks and crops of analysed beta cells have been binned to near 16 nm isotropic voxel size and are available for download via https://betaseg.github.io. The FIJI plugin *BetaSeg Viewer* and the plugin for importing KNOSSOS skeletons can be downloaded via the update site https://sites.imagej.net/betaseg.

Author contributions: Conceptualization—A. Müller, M. Solimena; Investigation—A. Müller, D. Schmidt, S. Pang, C.S. Xu, M. Weigert, JV D'Costa, S. Kretschmar, C. Münster, T. Kurth, F. Jug, H. Hess, M. Solimena; Formal Analysis—A. Müller, D. Schmidt, M. Weigert, JV D'Costa; Software-D. Schmidt; Visualization-D. Schmidt, A. Müller, M. Weigert; Writing—Original Draft—A. Müller, D. Schmidt, M. Weigert, M. Solimena; Writing—Review and Editing—A. Müller, D. Schmidt, C.S. Xu, M. Weigert, JV D'Costa, T. Kurth, F. Jug, H. Hess, M. Solimena; Funding acquisition—A. Müller, M. Solimena.

References

I. Belevich, M. Joensuu, D. Kumar, H. Vihinen, and E. Jokitalo. Microscopy Image Browser: A Platform for Segmentation and Analysis of Multidimensional Datasets. *PLOS Biol.*, 14(1): e1002340, Jan. 2016. ISSN 1545-7885. doi: 10.1371/journal.pbio.1002340. URL https://journals.plos.org/plosbiology/article?id=10.1371/journal.pbio.1002340. Publisher: Public Library of Science.

S. Berg, D. Kutra, T. Kroeger, C. N. Straehle, B. X. Kausler, C. Haubold, M. Schiegg, J. Ales, T. Beier, M. Rudy, K. Eren, J. I. Cervantes, B. Xu, F. Beuttenmueller, A. Wolny, C. Zhang, U. Koethe, F. A. Hamprecht, and A. Kreshuk. ilastik: interactive machine learning for (bio)image analysis. *Nat. Methods*, 16(12):1226–1232, Dec. 2019. ISSN 1548-7105. doi: 10.1038/s41592-019-0582-9. URL https://www.nature.com/articles/s41592-019-0582-9. Number: 12 Publisher: Nature Publishing Group.

A. E. Boyd, W. E. Bolton, and B. R. Brinkley. Microtubules and beta cell function: effect of colchicine on microtubules and insulin secretion in vitro by mouse beta cells. *J. Cell Biol.*, 92(2):425–434, Feb. 1982. ISSN 0021-9525. doi: 10.1083/jcb.92.2.425.

G. J. Brouhard and L. M. Rice. Microtubule Dynamics: an interplay of biochemistry and mechanics. *Nat. Rev. Mol. Cell Biol.*, 19(7):451–463, July 2018. ISSN 1471-0072. doi: 10.1038/s41580-018-0009-y. URL https://www.ncbi.nlm.nih.gov/pmc/articles/PMC6019280/.

C. Buser and P. Walther. Freeze-substitution: the addition of water to polar solvents enhances the retention of structure and acts at temperatures around -60 degrees C. *J. Microsc.*, 230(Pt 2): 268–277, May 2008. ISSN 1365-2818. doi: 10.1111/j.1365-2818.2008.01984.x.

K. Chabin-Brion, J. Marceiller, F. Perez, C. Settegrana, A. Drechou, G. Durand, and C. Poüs. The Golgi Complex Is a Microtubule-organizing Organelle. *Mol. Biol. Cell*, 12(7):2047–2060, July 2001. ISSN 1059-1524. doi: 10.1091/mbc.12.7.2047. URL https://www.molbiolcell.org/doi/full/10.1091/mbc.12.7.2047. Publisher: American Society for Cell Biology (mbc).

J. Cui, Z. Wang, Q. Cheng, R. Lin, X.-M. Zhang, P. S. Leung, N. G. Copeland, N. A. Jenkins, K.-M. Yao, and J.-D. Huang. Targeted inactivation of kinesin-1 in pancreatic β-cells in vivo leads to insulin secretory deficiency. *Diabetes*, 60(1):320–330, Jan. 2011. ISSN 1939-327X. doi: 10.2337/db09-1078.

H. de Forges, A. Bouissou, and F. Perez. Interplay between microtubule dynamics and intracellular organization. *Int. J. Biochem. Cell Biol.*, 44(2):266–274, Feb. 2012. ISSN 1357-2725. doi: 10.1016/j.biocel.2011.11.009. URL http://www.sciencedirect.com/science/article/pii/S1357272511003074.

P. M. Dean. Ultrastructural morphometry of the pancreatic β-cell. *Diabetologia*, 9(2):115–119, Apr. 1973. ISSN 1432-0428. doi: 10.1007/BF01230690. URL https://doi.org/10.1007/BF01230690.

A. Efimov, A. Kharitonov, N. Efimova, J. Loncarek, P. M. Miller, N. Andreyeva, P. Gleeson, N. Galjart, A. R. R. Maia, I. X. McLeod, J. R. Yates, H. Maiato, A. Khodjakov, A. Akhmanova, and I. Kaverina. Asymmetric CLASP-dependent nucleation of non-centrosomal microtubules at the trans-Golgi network. *Dev. Cell*, 12(6):917–930, June 2007. ISSN 1534-5807. doi: 10.1016/j.devcel.2007.04.002. URL https://www.ncbi.nlm.nih.gov/pmc/articles/PMC2705290/.

E. Fava, J. Dehghany, J. Ouwendijk, A. Müller, A. Niederlein, P. Verkade, M. Meyer-Hermann, and M. Solimena. Novel standards in the measurement of rat insulin granules combining electron microscopy, high-content image analysis and in silico modelling. *Diabetologia*, 55(4): 1013–1023, Apr. 2012. ISSN 1432-0428. doi: 10.1007/s00125-011-2438-4.

L. Fourriere, A. J. Jimenez, F. Perez, and G. Boncompain. The role of microtubules in secretory protein transport. *J. Cell Sci.*, 133(2), Jan. 2020. ISSN 0021-9533, 1477-9137. doi: 10.1242/jcs.237016. URL https://jcs.biologists.org/content/133/2/jcs237016. Publisher: The Company of Biologists Ltd Section: Review.

M. Gotoh, T. Maki, T. Kiyoizumi, S. Satomi, and A. P. Monaco. An improved method for isolation of mouse pancreatic islets. *Transplantation*, 40(4):437–438, Oct. 1985. ISSN 0041-1337. doi: 10.1097/00007890-198510000-00018.

D. H. Hall, E. Hartwieg, and K. Nguyen. WormAtlas Anatomical Methods - OTO Fixation for SEM Blockface Imaging. *WormAtlas*, Apr. 2013. doi: 10.3908/wormatlas.9.8. URL http://www.wormatlas.org/EMmethods/OTOFix.htm.

C. R. Harris, K. J. Millman, S. J. van der Walt, R. Gommers, P. Virtanen, D. Cournapeau, E. Wieser, J. Taylor, S. Berg, N. J. Smith, R. Kern, M. Picus, S. Hoyer, M. H. van Kerkwijk, M. Brett, A. Haldane, J. F. del Río, M. Wiebe, P. Peterson, P. Gérard-Marchant, K. Sheppard, T. Reddy, W. Weckesser, H. Abbasi, C. Gohlke, and T. E. Oliphant. Array programming with NumPy. *Nature*, 585(7825):357–362, Sept. 2020. ISSN 1476-4687. doi: 10.1038/

s41586-020-2649-2. URL https://www.nature.com/articles/s41586-020-2649-2. Number: 7825 Publisher: Nature Publishing Group.

J. J. Hartman, J. Mahr, K. McNally, K. Okawa, A. Iwamatsu, S. Thomas, S. Cheesman, J. Heuser, R. D. Vale, and F. J. McNally. Katanin, a Microtubule-Severing Protein, Is a Novel AAA ATPase that Targets to the Centrosome Using a WD40-Containing Subunit. *Cell*, 93(2):277–287, Apr. 1998. ISSN 0092-8674, 1097-4172. doi: 10.1016/S0092-8674(00)81578-0. URL https://www.cell.com/cell/abstract/S0092-8674(00)81578-0. Publisher: Elsevier.

A. T. Heaslip, S. R. Nelson, A. T. Lombardo, S. Beck Previs, J. Armstrong, and D. M. Warshaw. Cytoskeletal Dependence of Insulin Granule Movement Dynamics in INS-1 Beta-Cells in Response to Glucose. *PLoS ONE*, 9(10), Oct. 2014. ISSN 1932-6203. doi: 10.1371/journal.pone.0109082. URL https://www.ncbi.nlm.nih.gov/pmc/articles/PMC4195697/.

M. Helmstaedter, K. L. Briggman, and W. Denk. High-accuracy neurite reconstruction for high-throughput neuroanatomy. *Nat. Neurosci.*, 14(8):1081–1088, Aug. 2011. ISSN 1546-1726. doi: 10.1038/nn.2868. URL https://www.nature.com/articles/nn.2868. Number: 8 Publisher: Nature Publishing Group.

P. Hoboth, A. Müller, A. Ivanova, H. Mziaut, J. Dehghany, A. Sönmez, M. Lachnit, M. Meyer-Hermann, Y. Kalaidzidis, and M. Solimena. Aged insulin granules display reduced microtubule-dependent mobility and are disposed within actin-positive multigranular bodies. *Proc. Natl. Acad. Sci. USA*, 112(7):E667–676, Feb. 2015. ISSN 1091-6490. doi: 10.1073/pnas.1409542112.

J. D. Hunter. Matplotlib: A 2d graphics environment. *Computing in science & engineering*, 9(3): 90–95, 2007.

J. L. Höög, C. Schwartz, A. T. Noon, E. T. O'Toole, D. N. Mastronarde, J. R. McIntosh, and C. Antony. Organization of Interphase Microtubules in Fission Yeast Analyzed by Electron Tomography. *Dev. Cell*, 12(3):349–361, Mar. 2007. ISSN 1534-5807. doi: 10.1016/j.devcel.2007.01.020. URL https://www.cell.com/developmental-cell/abstract/S1534-5807(07)00018-4. Publisher: Elsevier.

K. Jiang, S. Hua, R. Mohan, I. Grigoriev, K. W. Yau, Q. Liu, E. A. Katrukha, A. F. M. Altelaar, A. J. R. Heck, C. C. Hoogenraad, and A. Akhmanova. Microtubule minus-end stabilization by polymerization-driven CAMSAP deposition. *Dev. Cell*, 28(3):295–309, Feb. 2014. ISSN 1878-1551. doi: 10.1016/j.devcel.2014.01.001.

M. A. Kalwat and D. C. Thurmond. Signaling mechanisms of glucose-induced F-actin remodeling in pancreatic islet β cells. *Exp. Mol. Med.*, 45(8):e37–e37, Aug. 2013. ISSN 2092-6413. doi: 10.1038/emm.2013.73. URL https://www.nature.com/articles/emm201373. Number: 8 Publisher: Nature Publishing Group.

J. R. Kremer, D. N. Mastronarde, and J. R. McIntosh. Computer visualization of three-dimensional image data using IMOD. *J. Struct. Biol.*, 116(1):71–76, Feb. 1996. ISSN 1047-8477. doi: 10.1006/jsbi.1996.0013.

B. J. Marsh, D. N. Mastronarde, K. F. Buttle, K. E. Howell, and J. R. McIntosh. Organellar relationships in the Golgi region of the pancreatic beta cell line, HIT-T15, visualized by high resolution electron tomography. *Proc. Natl. Acad. Sci. USA*, 98(5):2399–2406, Feb. 2001. ISSN 0027-8424, 1091-6490. doi: 10.1073/pnas.051631998. URL https://www.pnas.org/content/98/5/2399. Publisher: National Academy of Sciences Section: Biological Sciences.

M. L. McDaniel, C. G. Bry, R. W. Homer, C. J. Fink, D. Ban, and P. E. Lacy. Temporal changes in islet polymerized and depolymerized tubulin during biphasic insulin release. *Metabolism*, 29 (8):762–766, Aug. 1980. ISSN 0026-0495. doi: 10.1016/0026-0495(80)90200-0.

J. C. M. Meiring, B. I. Shneyer, and A. Akhmanova. Generation and regulation of microtubule network asymmetry to drive cell polarity. *Curr. Opin. Cell Biol.*, 62:86–95, Feb. 2020. ISSN 0955-0674. doi: 10.1016/j.ceb.2019.10.004. URL http://www.sciencedirect.com/science/article/pii/S0955067419300912.

Y. X. Meng, G. W. Wilson, M. C. Avery, C. H. Varden, and R. Balczon. Suppression of the expression of a pancreatic beta-cell form of the kinesin heavy chain by antisense oligonucleotides inhibits insulin secretion from primary cultures of mouse beta-cells. *Endocrinology*, 138(5): 1979–1987, May 1997. ISSN 0013-7227. doi: 10.1210/endo.138.5.5139.

M. M. Mogensen, A. Malik, M. Piel, V. Bouckson-Castaing, and M. Bornens. Microtubule minus-end anchorage at centrosomal and non-centrosomal sites: the role of ninein. *J. Cell Sci.*, 113 (Pt 17):3013–3023, Sept. 2000. ISSN 0021-9533.

A. Muroyama and T. Lechler. Microtubule organization, dynamics and functions in differentiated cells. *Development*, 144(17):3012–3021, 2017. ISSN 1477-9129. doi: 10.1242/dev.153151.

A. Müller, H. Mziaut, M. Neukam, K.-P. Knoch, and M. Solimena. A 4D view on insulin secretory granule turnover in the β-cell. *Diabetes Obes. Metab.*, 19 Suppl 1:107–114, 2017a. ISSN 1463-1326. doi: 10.1111/dom.13015.

A. Müller, M. Neukam, A. Ivanova, A. Sönmez, C. Münster, S. Kretschmar, Y. Kalaidzidis, T. Kurth, J.-M. Verbavatz, and M. Solimena. A Global Approach for Quantitative Super Resolution and Electron Microscopy on Cryo and Epoxy Sections Using Self-labeling Protein Tags. *Sci. Rep.*, 7(1):23, 2017b. ISSN 2045-2322. doi: 10.1038/s41598-017-00033-x.

F. M. Nixon, T. R. Honnor, N. I. Clarke, G. P. Starling, A. J. Beckett, A. M. Johansen, J. A. Brettschneider, I. A. Prior, and S. J. Royle. Microtubule organization within mitotic spindles revealed by serial block face scanning electron microscopy and image analysis. *J. Cell Sci.*, 130(10):1845–1855, May 2017. ISSN 0021-9533, 1477-9137. doi: 10.1242/jcs.203877. URL https://jcs.biologists.org/content/130/10/1845. Publisher: The Company of Biologists Ltd Section: TOOLS AND TECHNIQUES.

A. B. Noske, A. J. Costin, G. P. Morgan, and B. J. Marsh. Expedited approaches to whole cell electron tomography and organelle mark-up in situ in high-pressure frozen pancreatic islets. *J. Struct. Biol.*, 161(3):298–313, Mar. 2008. ISSN 1095-8657. doi: 10.1016/j.jsb.2007.09.015.

C. S. Olofsson, S. O. Göpel, S. Barg, J. Galvanovskis, X. Ma, A. Salehi, P. Rorsman, and L. Eliasson. Fast insulin secretion reflects exocytosis of docked granules in mouse pancreatic B-cells. *Pflugers Arch.*, 444(1):43–51, May 2002. ISSN 1432-2013. doi: 10.1007/s00424-002-0781-5. URL https://doi.org/10.1007/s00424-002-0781-5.

J. J. Park and Y. P. Loh. Minireview: How Peptide Hormone Vesicles Are Transported to the Secretion Site for Exocytosis. *Mol. Endocrinol.*, 22(12):2583–2595, Dec. 2008. ISSN 0888-8809. doi: 10.1210/me.2008-0209. URL https://www.ncbi.nlm.nih.gov/pmc/articles/PMC2626200/.

T. Pietzsch, S. Preibisch, P. Tomančák, and S. Saalfeld. Imglib2—generic image processing in java. *Bioinformatics*, 28(22):3009–3011, 2012.

T. Pietzsch, S. Saalfeld, S. Preibisch, and P. Tomancak. BigDataViewer: visualization and pro-

cessing for large image data sets. *Nat. Methods*, 12(6):481–483, June 2015. ISSN 1548-7105. doi: 10.1038/nmeth.3392. URL https://www.nature.com/articles/nmeth.3392. Number: 6 Publisher: Nature Publishing Group.

D. G. Pipeleers, M. A. Pipeleers-Marichal, and D. M. Kipnis. Microtubule assembly and the intracellular transport of secretory granules in pancreatic islets. *Science*, 191(4222):88–90, Jan. 1976. ISSN 0036-8075. doi: 10.1126/science.1108194.

A. E. Pouli, E. Emmanouilidou, C. Zhao, C. Wasmeier, J. C. Hutton, and G. A. Rutter. Secretory-granule dynamics visualized in vivo with a phogrin–green fluorescent protein chimaera. *Biochem. J.*, 333(1):193–199, July 1998. ISSN 0264-6021. doi: 10.1042/bj3330193. URL /biochemj/article/333/1/193/34154/Secretory-granule-dynamics-visualized-in-vivo-with. Publisher: Portland Press.

S. Redemann, J. Baumgart, N. Lindow, M. Shelley, E. Nazockdast, A. Kratz, S. Prohaska, J. Brugués, S. Fürthauer, and T. Müller-Reichert. C. elegans chromosomes connect to centrosomes by anchoring into the spindle network. *Nat. Commun.*, 8(1):15288, May 2017. ISSN 2041-1723. doi: 10.1038/ncomms15288. URL https://www.nature.com/articles/ncomms15288. Number: 1 Publisher: Nature Publishing Group.

A. Roll-Mecak and R. D. Vale. Structural basis of microtubule severing by the hereditary spastic paraplegia protein spastin. *Nature*, 451(7176):363–367, Jan. 2008. ISSN 0028-0836. doi: 10.1038/nature06482. URL https://www.ncbi.nlm.nih.gov/pmc/articles/PMC2882799/.

O. Ronneberger, P. Fischer, and T. Brox. U-net: Convolutional networks for biomedical image segmentation. In *International Conference on Medical image computing and computer-assisted intervention*, pages 234–241. Springer, 2015.

P. Rorsman and E. Renström. Insulin granule dynamics in pancreatic beta cells. *Diabetologia*, 46(8):1029–1045, Aug. 2003. ISSN 0012-186X. doi: 10.1007/s00125-003-1153-1.

R. Rudolf, T. Salm, A. Rustom, and H.-H. Gerdes. Dynamics of Immature Secretory Granules: Role of Cytoskeletal Elements during Transport, Cortical Restriction, and F-Actin-dependent Tethering. *Mol. Biol. Cell*, 12(5):1353–1365, May 2001. ISSN 1059-1524. URL https://www.ncbi.nlm.nih.gov/pmc/articles/PMC34589/.

C. T. Rueden, J. Schindelin, M. C. Hiner, B. E. DeZonia, A. E. Walter, E. T. Arena, and K. W. Eliceiri. Imagej2: Imagej for the next generation of scientific image data. *BMC bioinformatics*, 18(1):529, 2017.

C. Salinno, P. Cota, A. Bastidas-Ponce, M. Tarquis-Medina, H. Lickert, and M. Bakhti. β-Cell Maturation and Identity in Health and Disease. *Int. J. Mol. Sci.*, 20(21), Oct. 2019. ISSN 1422-0067. doi: 10.3390/ijms20215417. URL https://www.ncbi.nlm.nih.gov/pmc/articles/PMC6861993/.

A. A. W. M. Sanders and I. Kaverina. Nucleation and dynamics of Golgi-derived microtubules. *Front. Neurosci.*, 9, 2015. ISSN 1662-453X. doi: 10.3389/fnins.2015.00431. URL https://www.frontiersin.org/articles/10.3389/fnins.2015.00431/full. Publisher: Frontiers.

J. Schindelin, I. Arganda-Carreras, E. Frise, V. Kaynig, M. Longair, T. Pietzsch, S. Preibisch, C. Rueden, S. Saalfeld, B. Schmid, J.-Y. Tinevez, D. J. White, V. Hartenstein, K. Eliceiri, P. Tomancak, and A. Cardona. Fiji: an open-source platform for biological-image analysis. *Nat. Methods*, 9(7):676–682, July 2012. ISSN 1548-7105. doi: 10.1038/nmeth.2019. URL https://www.nature.com/articles/nmeth.2019. Number: 7 Publisher: Nature Publishing Group.

B. Schmid, P. Tripal, T. Fraaß, C. Kersten, B. Ruder, A. Grüneboom, J. Huisken, and R. Palmisano. 3Dscript: animating 3D/4D microscopy data using a natural-language-based syntax. *Nat. Methods*, 16(4):278–280, Apr. 2019. ISSN 1548-7105. doi: 10.1038/s41592-019-0359-1. URL https://www.nature.com/articles/s41592-019-0359-1. Number: 4 Publisher: Nature Publishing Group.

A. Shomorony, C. R. Pfeifer, M. A. Aronova, G. Zhang, T. Cai, H. Xu, A. L. Notkins, and R. D. Leapman. Combining quantitative 2D and 3D image analysis in the serial block face SEM: application to secretory organelles of pancreatic islet cells. *J. Microsc.*, 259(2):155–164, 2015. ISSN 1365-2818. doi: 10.1111/jmi.12276. URL https://onlinelibrary.wiley.com/doi/abs/10.1111/jmi.12276. _eprint: https://onlinelibrary.wiley.com/doi/pdf/10.1111/jmi.12276.

A. Varadi, E. K. Ainscow, V. J. Allan, and G. A. Rutter. Involvement of conventional kinesin in glucose-stimulated secretory granule movements and exocytosis in clonal pancreatic beta-cells. *J. Cell Sci.*, 115(Pt 21):4177–4189, Nov. 2002. ISSN 0021-9533.

A. Varadi, T. Tsuboi, L. I. Johnson-Cadwell, V. J. Allan, and G. A. Rutter. Kinesin I and cytoplasmic dynein orchestrate glucose-stimulated insulin-containing vesicle movements in clonal MIN6 β-cells. *Biochem. Biophys. Res. Commun.*, 311(2):272–282, Nov. 2003. ISSN 0006-291X. doi: 10.1016/j.bbrc.2003.09.208. URL http://www.sciencedirect.com/science/article/pii/S0006291X03020473.

P. Verkade. Moving EM: the Rapid Transfer System as a new tool for correlative light and electron microscopy and high throughput for high-pressure freezing. *J. Microsc.*, 230(2):317–328, 2008. ISSN 1365-2818. doi: 10.1111/j.1365-2818.2008.01989.x. URL https://onlinelibrary.wiley.com/doi/abs/10.1111/j.1365-2818.2008.01989.x. _eprint: https://onlinelibrary.wiley.com/doi/pdf/10.1111/j.1365-2818.2008.01989.x.

P. Virtanen, R. Gommers, T. E. Oliphant, M. Haberland, T. Reddy, D. Cournapeau, E. Burovski, P. Peterson, W. Weckesser, J. Bright, et al. Scipy 1.0: fundamental algorithms for scientific computing in python. *Nat. methods*, 17(3):261–272, 2020.

I. A. Vorobjev, T. M. Svitkina, and G. G. Borisy. Cytoplasmic assembly of microtubules in cultured cells. *J. Cell Sci.*, 110(21):2635–2645, Nov. 1997. ISSN 0021-9533, 1477-9137. URL https://jcs.biologists.org/content/110/21/2635. Publisher: The Company of Biologists Ltd Section: Journal Articles.

M. Weigert, U. Schmidt, R. Haase, K. Sugawara, and G. Myers. Star-convex Polyhedra for 3D Object Detection and Segmentation in Microscopy. *2020 IEEE Winter Conference on Applications of Computer Vision (WACV)*, pages 3655–3662, Mar. 2020. doi: 10.1109/WACV45572.2020.9093435. URL http://arxiv.org/abs/1908.03636. arXiv: 1908.03636.

Wes McKinney. Data Structures for Statistical Computing in Python. In Stéfan van der Walt and Jarrod Millman, editors, *Proceedings of the 9th Python in Science Conference*, pages 56 – 61, 2010. doi: 10.25080/Majora-92bf1922-00a.

C. S. Xu, K. J. Hayworth, Z. Lu, P. Grob, A. M. Hassan, J. G. García-Cerdán, K. K. Niyogi, E. Nogales, R. J. Weinberg, and H. F. Hess. Enhanced FIB-SEM systems for large-volume 3D imaging. *eLife*, 6:e25916, May 2017. ISSN 2050-084X. doi: 10.7554/eLife.25916. URL https://doi.org/10.7554/eLife.25916. Publisher: eLife Sciences Publications, Ltd.

C. S. Xu, K. J. Hayworth, and H. F. Hess. Enhanced FIB-SEM systems for large-volume 3D imaging, Mar. 2020a. URL https://patents.google.com/patent/US10600615B2/en. US Patent 10,600,615.

C. S. Xu, S. Pang, K. J. Hayworth, and H. F. Hess. Transforming fib-sem systems for large-volume connectomics and cell biology. In I. Wacker, E. Hummel, S. Burgold, and R. Schröder, editors, *Volume Microscopy : Multiscale Imaging with Photons, Electrons, and Ions*, Neuromethods, pages 221–243. Springer US, New York, NY, 2020b. ISBN 978-1-07-160691-9. doi: 10.1007/978-1-0716-0691-9_12. URL https://doi.org/10.1007/978-1-0716-0691-9_12.

C. S. Xu, S. Pang, G. Shtengel, A. Müller, A. T. Ritter, H. K. Hoffman, S.-y. Takemura, Z. Lu, H. A. Pasolli, N. Iyer, J. Chung, D. Bennett, A. V. Weigel, T. C. Walther, R. V. Farese, S. B. v. Engelenburg, I. Mellman, M. Solimena, and H. F. Hess. Isotropic 3D electron microscopy reference library of whole cells and tissues. *bioRxiv*, page 2020.11.13.382457, Nov. 2020c. doi: 10.1101/2020.11.13.382457. URL https://www.biorxiv.org/content/10.1101/2020.11.13.382457v1. Publisher: Cold Spring Harbor Laboratory Section: New Results.

A. M. Yvon and P. Wadsworth. Non-centrosomal microtubule formation and measurement of minus end microtubule dynamics in A498 cells. *Journal of Cell Science*, 110(19):2391–2401, Oct. 1997. ISSN 0021-9533, 1477-9137. URL https://jcs.biologists.org/content/110/19/2391. Publisher: The Company of Biologists Ltd Section: Journal Articles.

X. Zhang, X. Peng, C. Han, W. Zhu, L. Wei, Y. Zhang, Y. Wang, X. Zhang, H. Tang, J. Zhang, X. Xu, F. Feng, Y. Xue, E. Yao, G. Tan, T. Xu, and L. Chen. A unified deep-learning network to accurately segment insulin granules of different animal models imaged under different electron microscopy methodologies. *Protein Cell*, 10(4):306–311, Apr. 2019. ISSN 1674-8018. doi: 10.1007/s13238-018-0575-y. URL https://doi.org/10.1007/s13238-018-0575-y.

X. Zhu, R. Hu, M. Brissova, R. W. Stein, A. C. Powers, G. Gu, and I. Kaverina. Microtubules Negatively Regulate Insulin Secretion in Pancreatic β Cells. *Dev. Cell*, 34(6):656–668, Sept. 2015. ISSN 1878-1551. doi: 10.1016/j.devcel.2015.08.020.

Materials and Methods

Islet isolation and culture

Pancreatic islets of 9 weeks old C57BL/6 mice were isolated as previously described (Gotoh et al., 1985). They were cultured overnight in standard culture media (RPMI 1640 (Gibco) with 10% FBS, 20 mM HEPES, 100 U/ml each penicillin and streptomycin) containing 5.5 mM glucose. Prior to high pressure freezing the islets were subjected to 1 hr incubation in Krebs-Ringer buffer containing either 3.3 mM or 16.7 mM glucose. All animal experiments were carried out according to FELASA guidelines and recommendations and are covered by a respective license for those experiments from the local authorities. Facilities for animal keeping and husbandry are certified and available with direct access on campus in Dresden. Licenses for animal experiments are approved by the State Directorate Saxony under license number DD24.1-5131/450/6.

High pressure freezing, freeze substitution and embedding

Islets were frozen with a Leica EM ICE high pressure freezer (Leica Microsystems, Germany) and kept in liquid nitrogen until freeze substitution. They were substituted as previously published (Müller et al., 2017b) or according to a novel protocol: first the samples were substituted in a cocktail containing 2% osmiumtetroxide, 1% uranylacetate, 0.5% glutaraldehyde, 5% H_2O (according to (Buser and Walther, 2008)) in acetone with 1% methanol at -90°C for 24 hours. The temperature was raised to 0°C over 15 hours followed by 4 washes with 100% acetone for 15 min each and an increase in temperature to +22°C. Afterwards the samples were incubated in 0.2% thiocarbohydrazide in 80% methanol at RT for 60 min followed by 6×10 min washes with 100% acetone. The specimens were stained with 2% osmiumtetroxide in acetone at RT for 60 min followed by incubation in 1% uranylacetate in acetone + 10% methanol in the dark at RT for 60 min. After 4 washes in acetone for 15 min each they were infiltrated with increasing concentrations of Durcupan resin in acetone followed by incubation in pure Durcupan and polymerization at 60°C. For quality control the blocks were

sectioned with a Leica LC6 ultramicrotome (Leica microsystems) and 300 nm sections were put on slot grids containing a Formvar film. Tilt series ranging from -63° to +63° were acquired with a F30 electron microscope (Thermo Fisher) and reconstructed with the IMOD software package (Kremer et al., 1996).

FIB-SEM imaging

Prior to FIB milling small vertical posts were trimmed to the region of interest guided by X-ray tomography data obtained by a Zeiss Versa XRM-510 and optical inspection under a microtome. A thin layer of conductive material of 10-nm gold followed by 100-nm carbon was coated on the trimmed samples using a Gatan 682 High-Resolution Ion Beam Coater. The coating parameters were 6 keV, 200 nA on both argon gas plasma sources, 10 rpm sample rotation with 45-degree tilt. The coated samples were imaged using a customized FIB-SEM with a Zeiss Capella FIB column mounted at 90° onto a Zeiss Merlin SEM. Details of the enhanced FIB-SEM systems were previously described (Xu et al., 2017, 2020a,b). Each block face was imaged by a 140 pA electron beam with 0.9 keV landing energy at 200 kHz. The x-y pixel size was set at 4 nm. A subsequently applied focused Ga+ beam of 15 nA at 30 keV strafed across the top surface and ablated away 4 nm of the surface. The newly exposed surface was then imaged again. The ablation – imaging cycle continued about once every 3-4 minutes for 2 weeks to complete FIB-SEM imaging one sample. The sequence of acquired images formed a raw imaged volume, followed by post processing of image registration and alignment using a Scale Invariant Feature Transform (SIFT) based algorithm. The actual z-step was estimated by the changes of SEM working distance and FIB milling position (Xu et al., 2020c). Specifically, the voxel dimensions were 4×4×4.24 nm (low glucose volume) and 4×4×3.40 nm (high glucose volume). The image stacks were rescaled to form 4×4×4 nm isotropic voxels which can be viewed in any arbitrary orientations.

Segmentation of FIB-SEM data

Due to the differences in cell organelle morphology and involved length scales, segmentation of the different organelles poses specific challenges that we approached with a dedicated method for each organelle class: Large and contrast-rich organelles such as plasma membrane, nucleus, and mitochondria allowed fast semi-manual tracing or admitted relatively uncomplicated pixel-wise classification methods. The crowded distribution of insulin SGs and the convoluted structure of the Golgi complex required a two-stage process to first generate and curate training data for a subsequent final machine learning based segmentation step (details below). Microtubules posed the biggest segmentation challenge due to their small diameter (25 nm) and relatively low electron density. We thus opted in this case to perform laborious yet accurate manual tracing.

Microtubules: Traced manually by creating a skeleton with the KNOSSOS software (Helmstaedter et al., 2011). The original 4 nm isotropic voxel size of the dataset was used. Tracing was performed by two experts (AM and JVD'C). Final cor-

rections were done by AM. The final skeletons were scaled to reach a final microtubule thickness of 25 nm. The manual tracing and curating of the microtubule skeleton required approximately 50 h per cell.

Plasma membrane, nucleus, and centrioles: Segmented manually with Microscopy Image Browser (Belevich et al., 2016) using interpolation every 10 slices. Centrioles were roughly segmented followed by thresholding. The same was done for the nucleus.

Golgi apparatus: We used ilastik to create preliminary foreground mask of 10 crops (128×128×128 pixels each) from different cells. After manual curation these labeled crops were used to train a three-class U-Net (Ronneberger et al., 2015) which was then applied to all full volumes. We used data augmentation (flips, elastic deformations, Gaussian noise) during training. The volumes were binned by 4 resulting in 16 nm isotropic voxel size datasets.

Mitochondria: Segmented with ilastik (Berg et al., 2019) that employs a random forest classifier that predicts for every pixel the probability to belong either to the background or mitochondria class. Additionally we used the autocontext function of ilastik, which resulted in improved segmentation masks. The volumes were binned four-fold resulting in 16 nm isotropic voxel size datasets. Masks were then exported as hdf5 files.

Secretory Granules (SG): Deep learning has been succesfully applied to detect insulin SGs in 2D images (Zhang et al., 2019). Due to the packed and dense distribution of SGs accurate instance segmentation (*i.e.* assigning each SG a unique label) is very challenging. To address this, we first created preliminary instance masks with ilastik and a subsequent watershed transform and used them as preliminary groundtruth for training a 3D STARDIST model (Weigert et al., 2020). After one round of training with these preliminary (and imperfect) masks, we manually curated 5 small crops of the first STARDIST result (172×172×172 pixels each) that served as precise ground truth for the second and final round of STARDIST training. We used data augmentation (flips, elastic deformations, Gaussian noise, intensity shift) during training. The volumes were again binned four-fold resulting in 16 nm isotropic voxel size datasets.

Data analysis and visualisation

Segmentation postprocessing: Segmentation masks were first exported as hdf5 or Amira (am) files, then imported into FIJI and finally saved as Tiff files (Schindelin et al., 2012). Microtubule skeletons generated in KNOSSOS were imported into FIJI using a custom plugin and also saved as Tiff files.

Distance and connectivity calculations: Based on the segmentation and labeling data we calculated distance maps of organelle pixels and distance and connectivity relations between individual labels with ImageJ2 (Rueden et al., 2017) and ImgLib2 (Pietzsch et al., 2012). Microtubules were categorized as centrosomal if the distance of one of their ends to the centrioles was smaller than 200 nm. We considered a secretory granule (SG) to be associated with a microtubule if

the minimal distance between SG pixels and a microtubule was smaller than 20 nm. Microtubule ends were considered as connected to the Golgi if their distance was smaller than 20 nm.

Distribution plots: We used Python based tools (Harris et al., 2020; Wes McKinney, 2010; Hunter, 2007; Virtanen et al., 2020) to process and visualize all distributions. When plotting microtubule end distances, *e.g.* to the membrane, from the two ends of each microtubule only the one closer to the membrane was taken into account. To set the distributions of distance measurements into perspective, we additionally plotted the non-zero distance distribution of the respective organelle in the cell, excluding the volume occupied by the nucleus. For instance, when plotting the distance of microtubule ends to the Golgi, the second histogram line in black accounts for the distances of all pixels in the cell to the Golgi, excluding any pixels belonging to the nucleus or to the Golgi itself. If microtubule ends would be randomly located in the cell and if their positions would not correlate with the location of other organelles, their distribution should roughly match this plot. We refer to these plots as random distributions ρ_X where X signifies the organelle with respective to which the distances were calculated (*e.g.* ρ_{Golgi}, ρ_{MT}, etc).
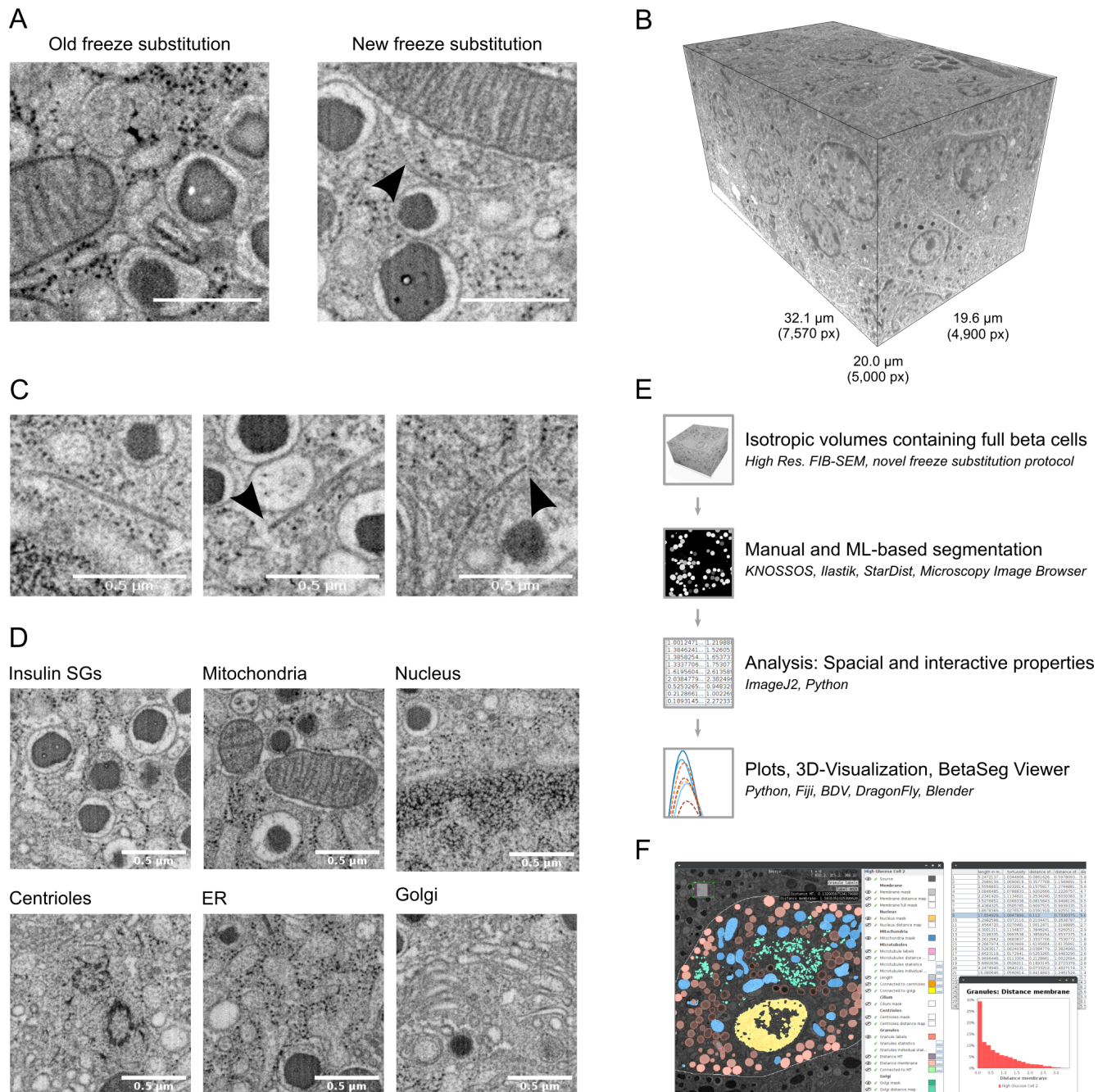
FIJI plugins: The plugins available in FIJI via our update site https://sites.imagej.net/betaseg, *BetaSeg Viewer* and the plugin for importing KNOSSOS skeletons, are both based on the SciJava plugin framework (https://scijava.org/). The viewer utilizes a preliminary version of LabelEditor (https://github.com/juglab/LabelEditor), a novel layer on top of BigDataViewer (Pietzsch et al., 2015) for displaying and interacting with labelings and label attributes. These attributes, *e.g.* microtubule length or distances between organelles, can directly be plotted with JFreeChart (http://www.jfree.org/jfreechart/).
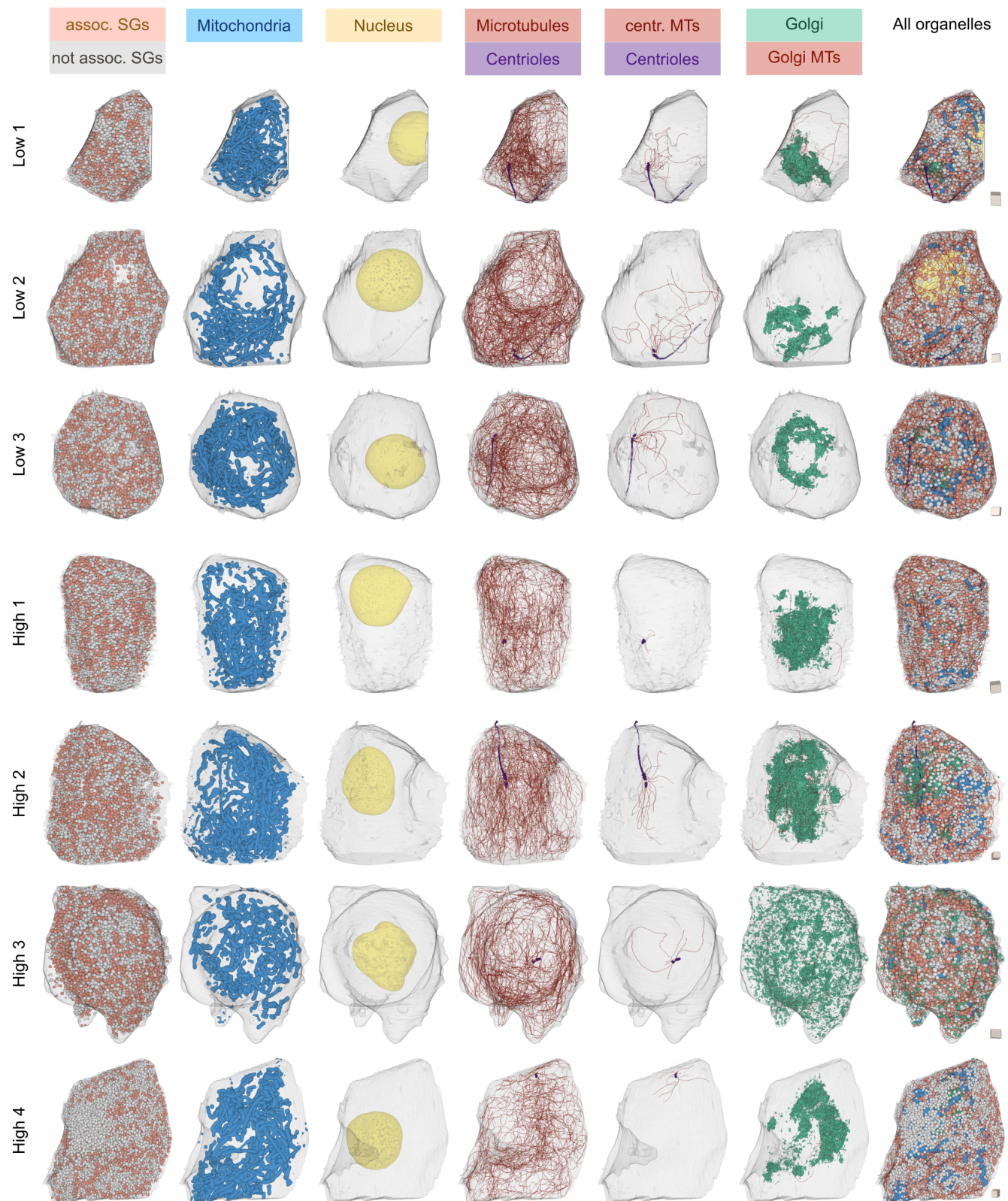
***BetaSeg Viewer* instructions:** FIJI/ ImageJ users can install the *BetaSeg Viewer* by adding the update site https://sites.imagej.net/BetaSeg via the Help>Update... in the menu. The data folder of at least one cell needs to be downloaded from https://betaseg.github.io. Afterwards one can start the viewer from the menu by clicking Analysis>BetaSeg and then pointing to the directory of one cell in the following popup. A new window with a BigDataViewer area on the left and a list of data components on the right will open, the EM source of the cell will be automatically displayed. The list of data components allows to interactively show or hide segmentations as well as analysis results, e.g. the length or tortuosity of microtubules. These properties are displayed via lookup tables (LUTs) in the viewer on top of the EM source. Colors can be adjusted. Individual values of e.g. single microtubules can be displayed by clicking the respective object. The analysis data can also be displayed as a histogram or table, available via the $\boxed{\cdots}$ button on the right of the specific data item.

Visualisation and 3D rendering: Overlays of raw data and segmentations were visualized with 3Dscript (Schmid et al., 2019). 3D rendering was done with the Dragonfly Software (theobjects.com/dragonfly) or blender (www.blender.org).
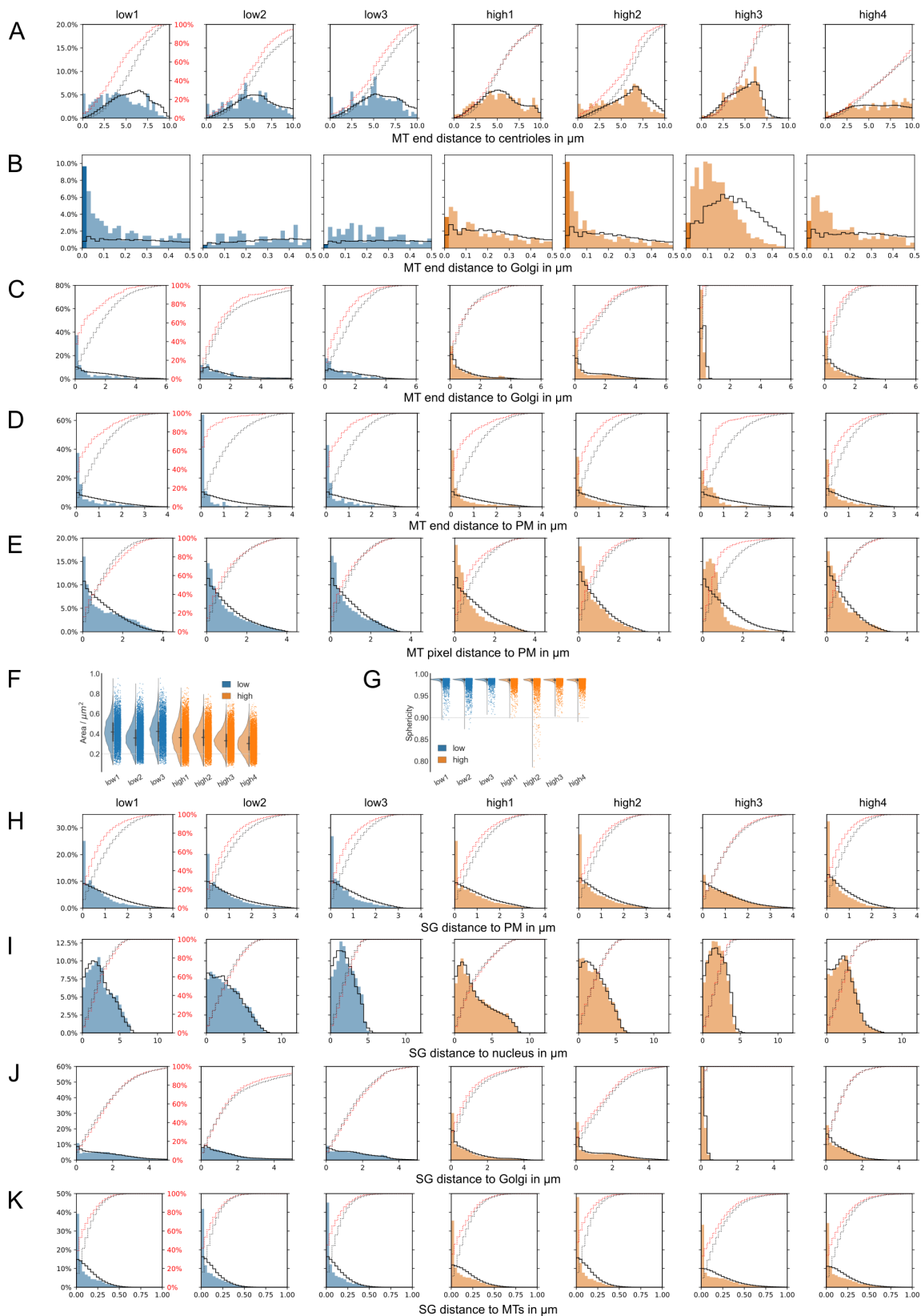
Supplementary Note 1: Supplementary Figures

Supplementary Figure 1. Raw FIB-SEM data and workflow for sample preparation, imaging, segmentation and data integration within *BetaSeg Viewer*. A) Snapshots of samples prepared according to the old and new freeze substitution protocol. Arrowhead: microtubule. Scalebar: 500 nm. **B)** Full raw volume of the low glucose dataset with pixel and μm dimensions. **C)** Detailed views of microtubules with arrowheads pointing to microtubule ends. **D)** Snapshots of ultrastructural details: Insulin SGs, mitochondria, nucleus, centrioles, endoplasmic reticulum (ER), Golgi apparatus. Scale bar: 500 nm. **E)** Workflow for sample preparation, imaging, segmentation and data integration within *BetaSeg Viewer*: Isotropic volumes of cryo-immobilized, freeze substituted and resin-embedded pancreatic islets were acquired with FIB-SEM followed by manual and machine-learning segmentation, 3D data analysis, integration into *BetaSeg Viewer* and 3D visualization. **F)** Screenshot of *BetaSeg Viewer* with an slice through an overlay of the raw volume of one beta cell with the corresponding segmentation masks, a table depicting quantitative data and a plot showing the distance of insulin SGs to the plasma membrane generated with *BetaSeg Viewer*.

Supplementary Figure 2. 3D renderings of all beta cells and organelles/organelle subtypes analysed in this study. Color coded are microtubule associated and not-associated SGs, mitochondria, nuclei, microtubules, centrioles, centrosomal microtubules, Golgi apparati, Golgi microtubules. Cubes on the right of each cell have a sidelength of 1 µm for scaling.

Supplementary Figure 3. Microtubule and SG analysis for all cells. A) Distance of microtubule ends to the nucleus. **B)** Distance of microtubule ends to Golgi (bin size 20 nm). **C)** Distance of microtubule ends to Golgi (bin size 200 nm). **D)** Distance of microtubule ends to plasma membrane. **E)** Distance of microtubule pixels to plasma membrane. **F)** Surface areas of SGs. **G)** Sphericity of SGs. **H)** Distance of SGs to plasma membrane. **I)** Distance of SGs to nucleus. **J)** Distance of SGs to Golgi apparatus. **K)** Distance of SGs to microtubules. Black lines in all distance distribution plots show the respective random distributions. Red dotted and black dotted lines represent actual and random cumulative distributions, respectively.

Supplementary Note 2: Supplementary Material

Supplementary Figure 1: Raw FIB-SEM data and processing and segmentation workflow.
Supplementary Figure 2: 3D renderings of all cells with organelles and organelle subsets.
Supplementary Figure 3: Plots for all analysed cells.
Video abstract: 3D animation of all segmented beta cells

Animation showing a raw FIB-SEM slice followed by the corresponding segmentation masks and a 3D rendering of the respective reconstructed beta cell. The individual organelles are highlighted followed by 3D renderings of all segmented cells.

Video 1: Raw FIB volume

Raw FIB-SEM volume corresponding to high glucose cell 1. Walking through the volume in z-direction reveals ultrastructural details such as insulin SGs, mitochondria, ER, ribosomes, the Golgi apparatus, the nucleus and microtubules. Scale bar: 500 nm.

Video 2: Beta cell microtubule and organelle segmentation

Raw FIB-SEM and corresponding 3D segmentation of one beta cell. Segmented plasma membrane, insulin SGs, mitochondria, Golgi apparatus, nucleus, centrioles and microtubules are shown in the color code used throughout the manuscript. Removal of insulin SGs, mitochondria and Golgi apparatus reveals the beta cell microtubule network.

Video 3: BetaSeg Viewer

Demonstration of the functionality of the BetaSeg Viewer FIJI plugin. It allows to load segmentation masks together with raw image stacks and to navigate through the data. The user can vizualize the different insulin SG categories and even obtain data of individual SGs.

Video 4: Microtubule network and centrosomal microtubules

Segmentation of centrosomal microtubules in comparison to all microtubules of one beta cell. Removal of non-centrosomal microtubules reveals the centrosomal microtubule subset of the cell.

Video 5: Microtubule network and Golgi-connected microtubules

Segmentation of Golgi-connected microtubules in comparison to all microtubules of one beta cell. Removal of non-Golgi microtubules reveals the Golgi-connected microtubule subset of the cell.

Video 6: Microtubule associated and not associated insulin SGs

Segmentation of microtubule associated and not associated insulin SGs of one cell. Removal of not associated SGs reveals the subset of microtubule connected SGs.

Videos can be viewed and downloaded via https://betaseg.github.io.